



Electrocatalytic upcycling of polyethylene terephthalate plastic to formic acid coupled with energy-saving hydrogen production over hierarchical Pd-doped NiTe nanoarrays

Hugang Zhang, Yile Wang, Xinmiao Li, Kai Deng, Hongjie Yu, You Xu, Hongjing Wang, Ziqiang Wang^{*}, Liang Wang^{*}

State Key Laboratory Breeding Base of Green-Chemical Synthesis Technology, College of Chemical Engineering, Zhejiang University of Technology, Hangzhou 310014, PR China

ARTICLE INFO

Keywords:

Upcycling PET plastic
Green hydrogen production
Electrocatalysis
Coupling strategy

ABSTRACT

Electrochemical upcycling of plastic waste to high-value chemicals is an ideal approach for the valorization of waste resources. In this study, we report the electro-reforming of polyethylene terephthalate (PET) plastic hydrolysate to valuable formate and hydrogen. Pd-deposited hierarchical aligned NiTe nanoarrays on Ni foam (Pd-NiTe/NF) is developed for oxidation of PET hydrolysate at anode and hydrogen evolution at cathode, with the overpotentials of 0.019 and 1.35 V at 10 and 100 mA cm⁻², respectively. In co-electrolysis system, the Pd-NiTe/NF exhibits high Faradaic efficiencies for concurrent production of value-added formate (95.6%) and H₂ (98.6%). The high activity and stability of Pd-NiTe/NF can be ascribed to that the interfacial heterostructures by incorporating Pd atoms and the strongly interfacial electronic interactions of between Pd and NiTe can synergistically promote PET-derived ethylene glycol to formate oxidation and hydrogen evolution. This work shows promising prospect in electro-reforming PET plastic waste to valuable chemicals.

1. Introduction

Plastic, as a momentous commercial and industrial material, has become a vital constituent of the contemporary lifestyle, with the annual global production of more than 380 million tons [1–3]. Polyethylene terephthalate (PET) is extensively utilized in food/beverage packaging, medical supplies, electronics, and polyester fibers, but it has relatively sluggish natural decomposition rate, resulting in severe environmental pollution [4–7]. Therefore, there is an urgent demand for effective strategies to degrade and recycle waste plastics. Currently, the techniques for recycling PET plastics waste consist of mechanical, biological, and chemical methods [8–11]. Among them, the chemical route exhibits significantly greater potential for upcycling PET plastics waste, in which PET plastics can be efficiently hydrolyzed into terephthalic acid (PTA) and ethylene glycol (EG) monomers under alkaline conditions [12–14]. The EG as an important source can be transformed into many valued products. Recently, it has been reported the transformation of PET waste into valued oxygenates (*i.e.*, formate, glyoxal, and acetate) by photocatalysis. However, this process suffers from low productivity and

selectivity towards single high-value oxidation product [15–17]. Therefore, electrocatalysis is expected to a promising technique to upcycle PET hydrolysate into high-value chemicals, but is still less explored.

In addition, hydrogen (H₂) is considered to be an incredibly promising energy carrier as it offers an energy-dense and carbon-neutral solution [18,19]. Electrocatalytic water splitting to produce hydrogen is a promising green hydrogen production technology, but it requires high energy input due to sluggish reaction kinetics of oxygen evolution reaction (OER) [20–22]. An impressive strategy of addressing this challenge is replacing the OER with small-molecule oxidation reactions that have greater thermodynamic favorability [23,24]. The small-molecule oxidation reactions are categorized into two types: electrochemical synthesis reactions (*e.g.*, the oxidation of alcohol and aldehyde) and sacrificial-agent oxidation reactions (*e.g.*, the oxidation of urea and hydrazine). Thereinto, electrochemical synthesis reactions are especially appealing due to the generation of hydrogen at the cathode, along with the production of high value-added products at the anode [25,26]. For instance, Wang et al. prepared high-performance PtRh_{0.02}@Rh

^{*} Corresponding authors.

E-mail addresses: zqwang@zjut.edu.cn (Z. Wang), wangliang@zjut.edu.cn (L. Wang).

<https://doi.org/10.1016/j.apcatb.2023.123236>

Received 8 June 2023; Received in revised form 24 August 2023; Accepted 27 August 2023

Available online 28 August 2023

0926-3373/© 2023 Elsevier B.V. All rights reserved.

nanowires electrocatalysts, which allowed EG to be used as the anodic feedstock to generate H_2 from seawater and obtained high-value biomass products with an ultralow cell voltage of 0.66 V at 10 mA cm^{-2} [27]. Based on the foregoing deliberations, an electrocatalytic strategy is exploited for the electrochemical valorization of PET waste to commodity chemicals (potassium diformate (KDF) and PTA) and concurrent production of hydrogen, as outlined in Fig. S1.

Recently, metal chalcogenides have been studied extensively as promising electrocatalysts due to their earth abundance and decent electrical conductivity [28–31]. For example, Liu and co-workers reported that a highly stable amorphous layer of noble metal chalcogenides catalysts ($PtSe_x$) exhibited the superior HER performance due to its robust single layer of noble metal and high atom-utilization efficiency [32]. In addition, Yang et al. synthesized the branched $NiSe_2$ nanoparticles, which could selectively convert EG to formate and simultaneously generate H_2 [33]. Nevertheless, the catalytic performances of various metal chalcogenides catalysts are insufficient for practical applications. To address this challenge, researchers are constantly exploring highly active electrocatalysts, which requires to optimize the adsorption behavior of the reaction intermediates on the material interface [34,35]. Interfacial engineering, as a promising strategy to modulate surface properties, can facilitate charge transfer between different components by constructing unique nano-interfaces and heterostructures, thus improving the catalyst performance [36–39]. In addition, the catalytic performance of materials can be enhanced by introducing low-content precious metals (e.g., Pd and Rh) to non-precious metals [40,41]. Therefore, engineering material interfaces by incorporating various phases to build heterostructures provides a promising approach to develop efficient electrocatalysts yet a formidable challenge.

Herein, we report the interfacial engineering of Pd-deposited hierarchical aligned NiTe nanoarrays on Ni foam (Pd-NiTe/NF) for coupling PET upcycling with HER. Originated from the characteristic structural advantages, the interfacial heterostructures by incorporating Pd atoms, and Pd with a upshifted d-band center and the strongly interfacial electronic interactions of between Pd and NiTe, the developed Pd-NiTe/NF possesses the exceptional performance for HER and PET hydrolysate oxidation, requiring overpotentials of 0.019 and 1.35 V at 10 and 100 mA cm^{-2} for HER and oxidation of PET hydrolysate, respectively, as well as high stability and Faradic efficiency. Moreover, in two-electrode co-electrolysis system, the Pd-NiTe/NF attains high Faradaic efficiencies for concurrent production of H_2 (98.6%) and the value-added formate (95.6%) at an optimal cell voltage.

2. Experimental section

2.1. Materials and chemicals

Sodium tellurite (Na_2TeO_3), palladium(II) chloride ($PdCl_2$), hydrochloric acid (HCl), hydrazine monohydrate ($N_2H_4 \cdot H_2O$), ascorbic acid (AA), ethylene glycol (EG) were purchased from Aladdin. Acetone and anhydrous ethanol were obtained from Shanghai Titan Scientific Co., Ltd. Nafion 117 solution (5 wt%) was purchased from Sigma-Aldrich. A certain concentration of H_2PdCl_4 solution was prepared by completely dissolving $PdCl_2$ in HCl solution.

2.2. Synthesis of NiTe nanoarrays on Ni foam

First, Ni foam (NF) was cut into small pieces of definite size ($4 \times 2 \times 0.2$ cm) and treated in HCl solution (3 M) by sonication for 15 min. Then, the NF was washed three times by deionized water and anhydrous ethanol, and dried at 50 °C for further use. The NiTe nanoarrays on NF (NiTe/NF) were prepared by the previous literature with small changes [42]. Typically, 0.4 g Na_2TeO_3 was thoroughly dissolved in 20 mL deionized water with vigorous stirring at room temperature. Subsequently, 11 mL $N_2H_4 \cdot H_2O$ was added slowly to the solution in

continuous stirring. After that, the above precursor solution was transferred to a Teflon-lined autoclave (50 mL) and a piece of pretreated NF was added, followed by heating the solution at 200 °C for 16 h. Finally, the resultant NiTe/NF was washed several times with ultrapure water and dried under vacuum at 50 °C for further use.

2.3. Synthesis of Pd modified NiTe nanoarrays on Ni foam

The Pd modified NiTe nanoarrays on Ni foam (Pd-NiTe/NF) were prepared via a wet chemical reduction method. In a typical procedure, the as-prepared NiTe/NF ($2 \times 2 \times 0.2$ cm) were immersed in a 4 mL H_2PdCl_4 aqueous solution (20 mM). Then, 2 mL of freshly prepared AA aqueous solution (0.1 M) was injected to above solution. The solution was placed at room temperature for 6 h to ensure complete reaction. Finally, the obtained Pd-NiTe/NF was washed with deionized water and dried under vacuum at 50 °C for further use.

2.4. Material characterizations

Scanning electron microscopy (SEM) was carried out to study the morphology of the samples on a ZEISS Gemini 500 at an accelerating voltage of 5 kV. Transmission electron microscopy (TEM), high-resolution TEM (HRTEM), high-angle annular dark-field scanning transmission electron microscopy (HAADF-STEM) and elemental mapping images were further performed to investigate the microstructure of catalysts on a Talos S-FEG with an acceleration voltage of 200 kV equipped with an energy dispersive X-ray (EDX) spectroscopy. The crystallographic data, surface electronic state and elemental composition of samples were investigated by employing X-ray powder diffraction (XRD, X'Pert PRO MPD) and X-ray photoelectron spectroscopy (XPS, Thermo Kalpha). 1H and ^{13}C nuclear magnetic resonance (NMR) spectra were conducted on a superconducting-magnet NMR spectrometer (Bruker AVANCE III HD 500 MHz).

2.5. Electrochemical investigations

All the electrochemical experiments were carried out at room temperature using CHI 660E electrochemical workstation. For all measurements, the potentials were calibrated with reference to a reversible hydrogen electrode (RHE) according to the Nernst equation:

$$E_{RHE} = E_{Hg/HgO} + 0.0977 \text{ V} + 0.059 \times pH \quad (1)$$

2.5.1. HER measurement

The HER tests were performed in 1.0 M KOH solution using a standard three-electrode system. The as-prepared catalyst ($1 \times 1 \times 0.2$ cm), a graphite rod and Hg/HgO electrode were served as the working electrode, the counter electrode and reference electrode, respectively. Before the HER test, the cyclic voltammetry (CV) measurements were carried out for 100 cycles at a scan rate of 50 mV s^{-1} to optimize the electrochemical accessibility of the working electrode. Linear sweep voltammetry (LSV) curves were conducted at a scan rate of 5 mV s^{-1} . All polarization curves achieved steady-state ones undergoing several cycles and recorded with iR correction. The Tafel plots were acquired from fitted LSV regions of overpotential against the logarithm of current density, based on Tafel equation [43]:

$$\eta = a \log j + b \quad (2)$$

where η is the overpotential, a is the Tafel slope, and j is the current density. The electrochemical impedance spectroscopy (EIS) was performed in the frequency ranging from 10^5 Hz to 0.1 Hz with a peak-to-peak sinusoidal potential perturbation. The electrochemical double layer capacitance (C_{dl}) was performed by CV curves at different scan rates from 20 to 120 mV s^{-1} . The long-term durability testing of the

catalyst was measured by chronopotentiometric ($V-t$) at a fixed current density of 100 mA cm^{-2} for 25 h.

For the Faradaic efficiency (FE) measurements, a water-gas displacing approach at room temperature was carried out to determine FE according to monitor the experimental amount of H_2 evolved during a 60 min electrocatalytic process. The FE was evaluated by the experimental number of moles of the gas and the theoretical number of moles of the gas. The theoretical molarity of the gas can be determined by using the following equation [44]:

$$n_{\text{g}}(\text{theoretical}) = Q/zF \quad (3)$$

Where n is the moles of generated gas, Q is the charge flowing through the electrodes, z presents mole electrons per mole H_2 ($z = 2$), F is Faraday constant (96485 C mol^{-1}). Consequently, the FE of H_2 can be calculated according to the following equation:

$$\text{FE} = n_{\text{g}}(\text{experimental})/n_{\text{g}}(\text{theoretical}) \quad (4)$$

2.5.2. PET hydrolysate oxidation measurement

PET hydrolysate was first prepared as the electrolyte by processing the obsoleted plastic. Typically, the discarded PET plastic bottles (8 g) were cut into pieces and added to 200 mL KOH solution (4 M). After successive heating for 84 h in an oil bath at 90°C , PET hydrolysate of 1 M potassium hydroxide was yielded by diluting the reaction solution. And the concentration EG concentration in PET hydrolysate is determined to be approximately 0.563 M by internal standard normalization. The electrocatalytic properties of PET hydrolysate oxidation were assessed by employing the standard three electrodes with as-prepared catalysts/NF ($1 \times 1 \times 0.2 \text{ cm}$) as the working electrode and a graphite rod as the counter electrode and Hg/HgO electrode as the reference electrode. The LSV curves were also performed at a scan rate of 5 mV s^{-1} . Amperometric ($i-t$) curve was conducted to assess the PET hydrolysate oxidation performance of Pd-NiTe/NF catalyst at different potentials for 2 h. The EGOR test was performed in 1 M KOH containing 0.5 M EG.

To quantify the concentration of the target product formate in the electrolysis product, PET hydrolysate (0.5 mL) after electrochemical oxidation at various potentials and deuterium oxide (D_2O) solution (0.1 mL) containing 5 mg mL^{-1} maleic acid (internal standard) were mixed. The ^1H NMR spectra of the above mixed solutions were obtained by NMR. The FE and productivity of formate were determined by using the following equation:

$$\text{FE} = zF\bar{c}/Q \quad (5)$$

$$\text{Formate productivity} = \frac{\text{Amount of produced formate}}{\text{Area of anode} \times \text{reaction time}} \quad (6)$$

Where c is the molar concentrations of formate, z is the number of electrons transferred, V is the electrolyte volume, F is the Faraday constant (96485 C mol^{-1}), and Q is the total charge during electrolysis.

2.5.3. HER coupling with PET hydrolysate oxidation measurement

The HER coupling with PET hydrolysate oxidation was performed in a two-electrode cell using Pd-NiTe/NF as both anode and cathode. The FE of H_2 and formate was analyzed according to Eqs. (4) and (5).

3. Results and discussion

The fabrication process of 3D hierarchical Pd-NiTe/NF nanoarrays heterostructure is schematically illustrated in Fig. 1, which is composed of two steps. For the first step, the hierarchical NiTe nanoarrays heterostructures supported on Ni foams are prepared by using Na_2TeO_3 as source of Te and N_2H_4 as the reducing agent to form NiTe in a hydrothermal approach. Scanning electron microscopy (SEM) and transmission electron microscopy (TEM) demonstrate that NiTe/NF possesses

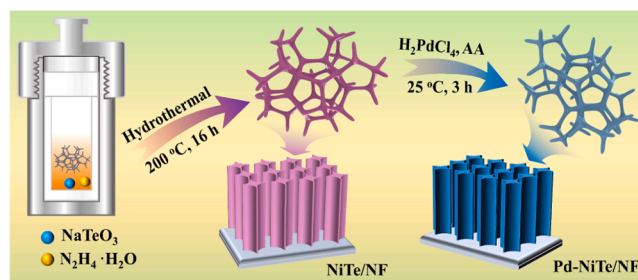


Fig. 1. Schematic illustration of the fabrication process of Pd-NiTe/NF.

cross column-like arrays architectures, which are homogeneously spread over the nickel foam (Fig. S2 and S3a). High-resolution TEM (HRTEM) image manifests the lattice interplanar spacings of 0.3 nm, which is corresponded to (101) facet of NiTe. Furthermore, high-angle annular dark-field scanning transmission electron microscopy (HAADF-STEM) image the EDX elemental mapping images of NiTe/NF present an orderly distribution of Ni and Te elements in the sample (Fig. S3b and c). Subsequently, the well-developed NiTe/NF serves as substrate materials for the construction of hierarchical Pd-NiTe/NF nanoarrays heterostructures through a facile wet-chemical reduction method using AA as reductant.

The morphological structures of Pd-NiTe/NF catalyst were initially unveiled by SEM. As depicted in Fig. 2a-c, the obtained Pd-NiTe/NF possesses the uniform morphology with hierarchical cross column-like nanoarrays with average diameter of about 60 nm, which are vertically distributed and inter-bridged with each other on the substrate of Ni foam. Moreover, a side-view SEM image proves that Pd-NiTe/NF is vertically grown on the NF surface with the average height of about $1.2 \mu\text{m}$ (Fig. S4). The detailed microstructure of Pd-NiTe/NF was further investigated by TEM. Fig. 2d exhibits a typical individual nanorod with the length of approximately 420 nm and affirms the rod-shaped structure of Pd-NiTe/NF. In particular, the morphology of Pd-NiTe/NF is maintained well compared to NiTe/NF, but the surface of Pd-NiTe/NF becomes obviously rougher and the diameter of nanorod becomes apparently thicker, demonstrating the successful incorporation of Pd layers on the surface of NiTe/NF, which is confirmed by TEM image (Fig. 2e). The HRTEM image of Pd-NiTe/NF displays two sets of lattice fringes with interplanar distances of 0.285 and 0.22 nm, which can be assigned to the (101) plane of NiTe and (111) plane of Pd, respectively, confirming the formation of hetero-structural Pd-NiTe structure (Fig. 2f). Noteworthy, the interplanar lattice spacing of NiTe in Pd-NiTe/NF is slightly smaller than that in NiTe/NF (0.3 nm), demonstrating the introduction of Pd atoms can induce the lattice contraction. The HAADF-STEM image and corresponding elemental mapping of Pd-NiTe/NF Fig. 2g, exhibits that the elements of Pd, Ni, and Te are uniformly dispersed throughout the whole structure, and the atomic ratio of Pd, Ni, and Te in the hierarchical Pd-NiTe/NF sample is determined to be around 4.6/48.9/46.5 by EDS spectrum (Fig. S5). These results demonstrate the successful preparation of hierarchical Pd-NiTe/NF nanoarrays heterostructure and Pd/NiTe interfaces.

X-ray diffraction (XRD) measurements were implemented to characterize the crystallographic structure of the samples. As presented in Fig. 3a, the XRD patterns demonstrate the formation of NiTe (JCPDS card No. 89–2018, space group $\text{P6}_3/\text{mmc}$). However, there are no distinct diffraction peaks associated with Pd in the XRD pattern of Pd-NiTe/NF due to the low-content of Pd on the surface of the Pd-NiTe/NF catalyst. In addition, the diffraction peaks of metallic Ni are derived from Ni foam substrate. The surface chemical constituents and valence states of the samples were further investigated by X-ray photoelectron spectroscopy (XPS) technology. As expected, the elements of Ni and Te can be scrutinized in the full spectrum of NiTe/NF. After the chemical reduction process, signal for Pd element is observed in the XPS survey spectrum of Pd-NiTe/NF (Fig. S6), manifesting that the surface of

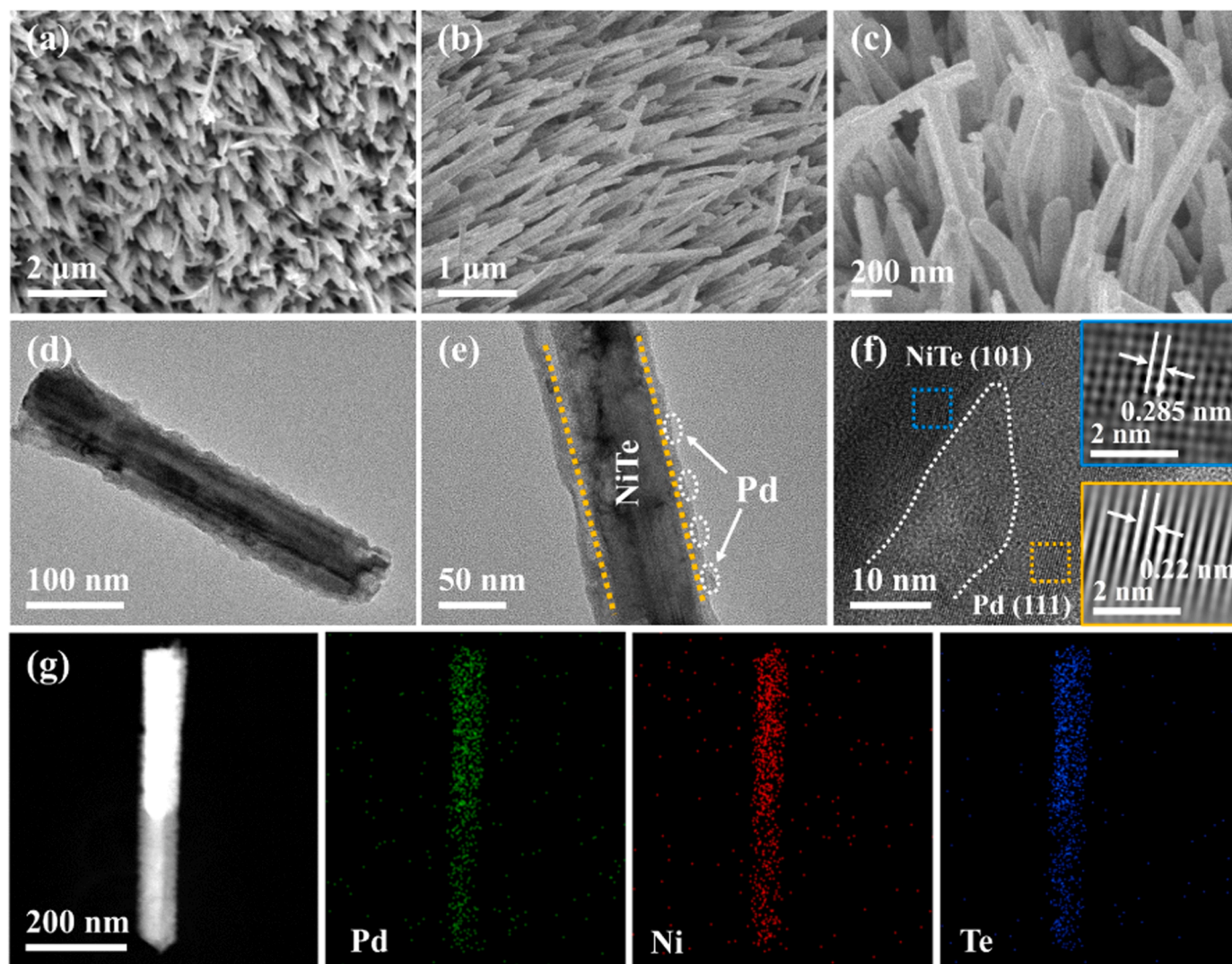


Fig. 2. (a–c) SEM, (d and e) TEM and (f) HRTEM images of Pd-NiTe/NF. Insets of (f) are the corresponding the Fourier filtered lattices of square areas. (g) HAADF-STEM image and corresponding elemental mapping images of Pd-NiTe/NF.

NiTe/NF have been successfully decorated by Pd atoms. With regards to the high-resolution Ni 2p spectra of Pd-NiTe/NF (Fig. 3b), two prominent peaks are deconvoluted into two spin-orbit doublets positioned at the binding energies of 873.18 and 855.48 eV, which can be assigned to the Ni 2p_{1/2} and Ni 2p_{3/2} of Ni(II), respectively, accompanied with two corresponding satellite peaks at 879.38 and 861.28 eV. The other faint peak at 852.18 eV pertains to the state of Ni(0) derived from NF substrate [45,46]. Conspicuously, the peaks of Ni 2p for Pd-NiTe/NF possess a positively deviation of ca. 0.18 eV toward higher binding energy compared with that for NiTe/NF, demonstrating a strong electronic interaction between Pd and NiTe. In the core-level Te 3d spectrum of NiTe (Fig. 3c), two fitted peaks situated at 586.08 and 575.58 eV can be attributed to the Te 3d_{3/2} and Te 3d_{5/2} of TeO_x, respectively, while the other weak peaks at 582.48 eV (Te 3d_{3/2}) and 582.88 eV (Te 3d_{5/2}) are appointed to the Te(0) [47,48]. Similarly, the Te 3d_{3/2} and Te 3d_{5/2} of Pd-NiTe/NF are positively shifted by 0.2 eV compared to those of pure NiTe/NF, corroborating partial electron depletion after Pd layer decoration. In addition, the XPS spectrum of Pd 3d toward Pd-NiTe/NF has two sets of pronounced diffraction peaks (Fig. 3d), the dominant peaks located at 340.68 and 335.38 eV can be indexed to the Pd 2p_{3/2} and Pd 2p_{5/2} of metallic Pd, respectively, while the surplus peaks at 343.28 (Pd 3d_{3/2}) and 336.48 eV (Pd 3d_{5/2}) correspond to the Pd(II) [49,50]. Furthermore, the binding energies of Pd 2p_{5/2} of metallic Pd in

Pd-NiTe/NF have a negatively deviation of 0.6 eV relative to that of the pure Pd/C, revealing that the partial electrons are concentrated in Pd and the interfacial charges are conveyed to Pd from Ni and Te, which can induce the upshift of the d-band center of Pd. Collectively, these analytical results illustrate the strongly interfacial electronic interactions between Pd layer and NiTe heterostructure, which makes it possible to modulate the electrocatalytic properties.

Based on the exceptional morphological structure and compositional characteristics, the electrocatalytic performances of the cathodic Pd-NiTe/NF for HER were first explored in 1.0 M KOH electrolyte using a typical three-electrode cell. As benchmarks, the electrocatalytic activities of pure NiTe/NF and bare NF were also assessed under identical conditions. As presented in Fig. 4a and Fig. S7, of all the polarization curves, the Pd-NiTe/NF electrode has a reduced overpotential and an increased current density relative to pure NiTe/NF and bare NF in 1.0 M KOH electrolyte, indicating that the decorated Pd interface is critical to improving the HER performance. To provide an accurate account of the catalytic activities of these materials, the overpotentials at a current density of 10, 50, 100, and 200 mA cm⁻² are obtained from LSV curves (Fig. 4b). Impressively, a 19 mV overpotential suffices for the Pd-NiTe/NF sample to yield a current density of 10 mA cm⁻², while the pure NiTe/NF and bare NF require overpotentials of 29 and 46 mV, respectively. Moreover, the Pd-NiTe/NF electrode necessitates an

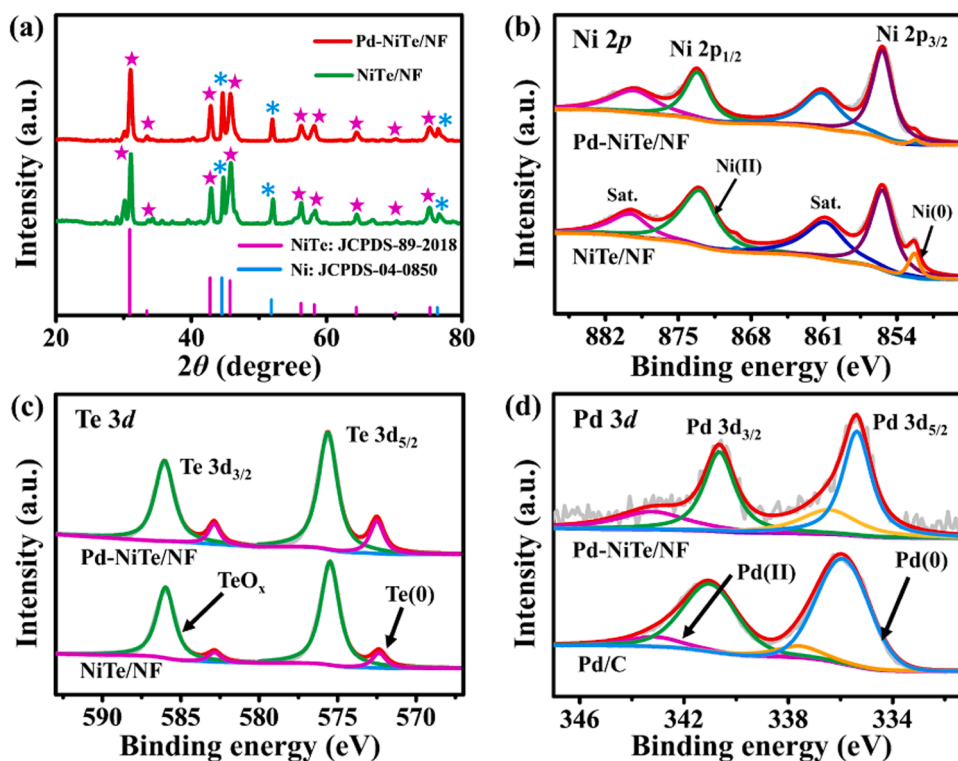


Fig. 3. (a) XRD patterns of Pd-NiTe/NF and NiTe/NF. The high-resolution XPS spectra of (b) Ni 2p, (c) Te 3d, and (d) Pd 3d for samples.

overpotential of 122 mV to achieve a high current density of 200 mA cm^{-2} , which is markedly less than that of pure NiTe/NF (155 mV). This is because the incorporation of Pd could regulate the interfacial electronic structure between Pd and NiTe to ameliorate the adsorption and activation of reactants, thereby facilitating the electrochemical performances of the resultant catalyst. It should be emphasized that Pd-NiTe/NF exhibits higher electrocatalytic activity than most reported HER catalysts (Table S1). To comprehend the HER reaction kinetics of electrocatalysts, the Tafel plots fitted from LSV curves can be used to estimate Tafel slope using the Eq. (2). As shown in Fig. 4c, the Pd-NiTe/NF has the lowest Tafel slope of 84.5 mV dec^{-1} , which is much smaller than those of pure NiTe/NF (92.8 mV dec^{-1}) and bare NF ($124.8 \text{ mV dec}^{-1}$), implying the remarkably enhanced kinetics and following a Volmer-Heyrovsky mechanism during the HER process. The exchange current density (j_0) was derived from the extrapolation of Tafel plots an overpotential of 0 V, reflecting the electron transfer competence of an electrode reaction. The j_0 value of Pd-NiTe/NF is estimated to be 5.89 mA cm^{-2} , larger than those of NiTe/NF (4.68 mA cm^{-2}) and bare NF (4.27 mA cm^{-2}), suggesting the boosted electron transfer rates. Electrochemical impedance spectra (EIS) were implemented to gain a more detailed comprehension of charge transfer process over the electrode/electrolyte interface behavior. Fig. 4d exhibits the Nyquist plots of the electrocatalysts with the equivalent resistor-capacitor circuit model (inset of Fig. 4d), where the uncompensated solution resistance (R_s) and charge-transfer resistance (R_{ct}) are used to represent the measured impedances in the high and middle/low frequency regions, respectively. The EIS spectrum of Pd-NiTe/NF displays the smaller semicircular arc relative to pure NiTe/NF and bare NF, and the R_{ct} of Pd-NiTe/NF is determined to be 1.15Ω (Table S2), which is substantially smaller than those of NiTe/NF (3.29Ω) and NF (8.47Ω). This unambiguous evidence corroborates that hierarchical Pd-NiTe/NF nanoarrays heterostructure possesses the smaller charge transfer resistance and higher charge transfer coefficient due to the enhanced charge transport along the hierarchically ordered array of Pd-NiTe/NF structure after the introduction of Pd atom layers, which contribute to the favorable electrocatalytic HER activity. To furthermore unveil the

intrinsic activity and the origin of the exceptional HER performance of hierarchical Pd-NiTe/NF nanoarrays catalyst, the double-layer capacitance (C_{dl}) of the catalysts was measured by CV curves in the non-faradaic region varying scanning rates from 20 to 120 mV s^{-1} to determine the counterpart electrochemical active surface areas (ECSA). As depicted in Fig. S8, the C_{dl} value of Pd-NiTe/NF is determined to be 13.4 mF cm^{-2} , which is rather larger than those of NiTe/NF (10.4 mF cm^{-2}) and NF (7.7 mF cm^{-2}). Consequently, the ECSA values of Pd-NiTe/NF, NiTe/NF, and NF are calculated to be 335, 260, and 192.5 cm^2 , respectively, revealing the opulently exposed active sites by directly Pd decoration on the 3D hierarchical nanoarray architecture and the intrinsic activity for the electrocatalytic process. In addition, the evolved H_2 from the cathodic Pd-NiTe/NF was collected by a water-gas displacing protocol. As shown in Fig. 4e, the hydrogen yield is almost identical to the H_2 obtained by the cumulative charge calculation during the HER process. The Faradic efficiency of Pd-NiTe/NF for H_2 generation is determined to be 99.1% through the Eq. (4) in alkaline electrolyte, indicating the superior HER activities. Along with the aim of achieving augmented catalytic performances, long-term electrochemical endurance is also a crucial aspect for electrocatalysts. The chronopotentiometric ($V-t$) measurement were carried out to evaluate the electrocatalytic stability of Pd-NiTe/NF. As shown in Fig. 4f, the $V-t$ curve at a constant current density of 100 mA cm^{-2} appears a negligible degradation of the overpotentials by comparing with the initial position after a long period of 25 h test, manifesting the decent durability of Pd-NiTe/NF catalyst.

For PET oxidative upcycling at the anode, the electrochemical performances of the diluted PET hydrolysate for Pd-NiTe/NF were investigated using a typical three-electrode configuration. Before PET hydrolysate oxidation, the performances of OER and EGOR were first measured to investigate the response activity of the as-synthesized catalysts for electro-oxidation of ethylene glycol. As displayed in Fig. S9, the Pd-NiTe/NF possesses an increase in the current density for OER from 1.39 V vs. RHE and requires an applied anodic potential of 1.47 V vs. RHE to drive the OER at a current density of 100 mA cm^{-2} in 1.0 M KOH. Upon the inclusion of EG in the KOH electrolyte, the Pd-NiTe/NF

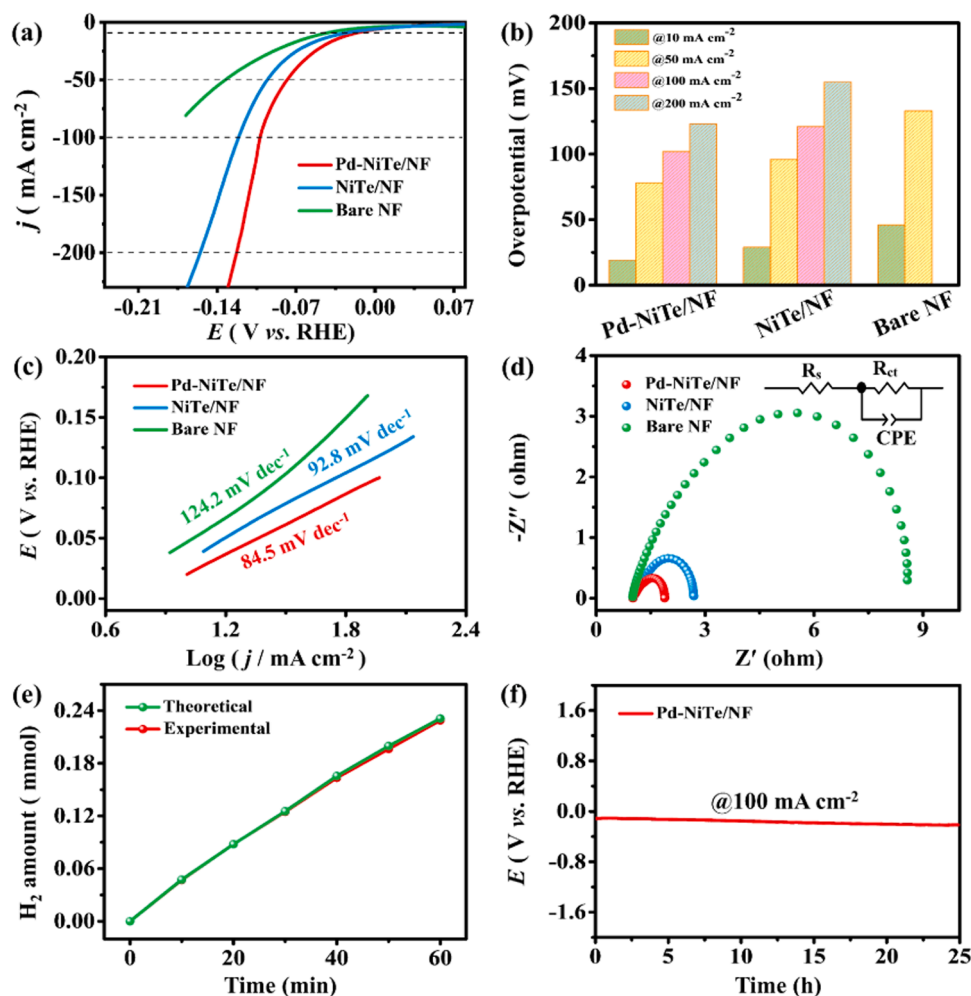


Fig. 4. (a) HER polarization curves of different samples and corresponding (b) overpotentials at 10, 50, 100, and 200 mA cm⁻² and (c) Tafel plots. (d) Nyquist plots of samples. (e) Comparison of the evolved hydrogen volume with the theoretical hydrogen volume. (f) V-t curve of the Pd-NiTe/NF at 100 mA cm⁻² for 25 h.

displays a lower onset potential of 1.28 V vs. RHE and an observable increase in the current density of EGOR (Fig. S10). Apparently, achieving the current density of 100 mA cm⁻² for EGOR only requires potential of 1.37 V vs. RHE, which are notably inferior to those for driving the OER, implying the thermodynamically more viable EGOR process over Pd-NiTe/NF. Moreover, it is worth noting that Pd-NiTe/NF exhibits higher activity and smaller Tafel slope than NiTe/NF and bare NF for both OER and EGOR (Fig. S9b and S10b), which is in agreement with the observation during the HER. In addition, after normalizing by ECSA for the diverse samples, Pd-NiTe/NF still exhibits a much higher current density compared with NiTe/NF and NF (Fig. S11), which further indicates that the enhanced activity in Pd-NiTe/NF is due to the more exposed active sites by incorporating Pd on the 3D hierarchical NiTe nanoarray architecture.

Based on the preceding discussion, the PET plastic hydrolysate was employed as the electrolyte to explore the electrocatalytic upcycling of PET hydrolysate for Pd-NiTe/NF. Fig. 5a displays the LSV curves of Pd-NiTe/NF performed in PET hydrolysate and 1.0 M KOH solution, which features a very comparable EGOR profile. The Pd-NiTe/NF catalyst exhibits an onset at ~1.21 V vs. RHE and a dramatic increase in current density for PET hydrolysate oxidation. To attain a current density of 100 mA cm⁻², the potential of Pd-NiTe/NF only requires 1.35 V to drive PET oxidation, which is 174 mV lower than that in 1.0 M KOH for OER, manifesting that the PET upcycling on Pd-NiTe/NF electrode is much easier to occur and more energy-saving than that of OER. It can be observed that the polarization curve has a small wave peak at ~1.28 V

vs. RHE arising from oxidation of Ni²⁺ to Ni³⁺, indicating the conversion of Ni from its lower to higher valence oxidation state and Ni³⁺ as the active center could be more suitable to the electrochemical oxidation of organic molecules [51,52]. Simultaneously, to explore the influence of reactants engaged in the electrochemical oxidation process in PET hydrolysate, the LSV curves of Pd-NiTe/NF electrode were conducted under different conditions (Fig. S12). In the presence of EG, the current density of Pd-NiTe/NF is greater than that in its absence at the same potential. Additionally, the electrochemical oxidation of EG is not compromised in the presence of PTA. Therefore, it is inferred that the Pd-NiTe/NF electrode can proficiently carry out the electrooxidation of EG in PET hydrolysate. Subsequently, ¹H and ¹³C NMR spectroscopy were utilized to qualitatively and quantitatively analyze the PET hydrolysate and its electro-reformed products. Fig. 5b shows the ¹H NMR spectra of PET hydrolysate and post-electrolysis PET hydrolysate performed by the chronoamperometry at diverse potentials (1.28, 1.33, 1.38, 1.43 and 1.48 V) for 2 h. As observed, the ¹H NMR spectrum of PET hydrolysate exhibits four main peaks corresponding to PTA (~7.78 ppm, green shaded) and EG (~3.5 ppm, yellow shaded), both from the hydrolysis of PET waste plastics in alkaline environment, while the peaks of formate at 8.35 ppm (blue shaded) can be detected in the ¹H NMR after the electrooxidation products of PET hydrolysate at different potentials. And the Faradaic efficiency of formate (FE_{formate}) is determined at different potentials by serving maleic acid (5.82 ppm, pink shaded) as an internal standard. The pre-electrolysis PET hydrolysate is also detected by ¹H NMR spectrum to demonstrate the conversion PET

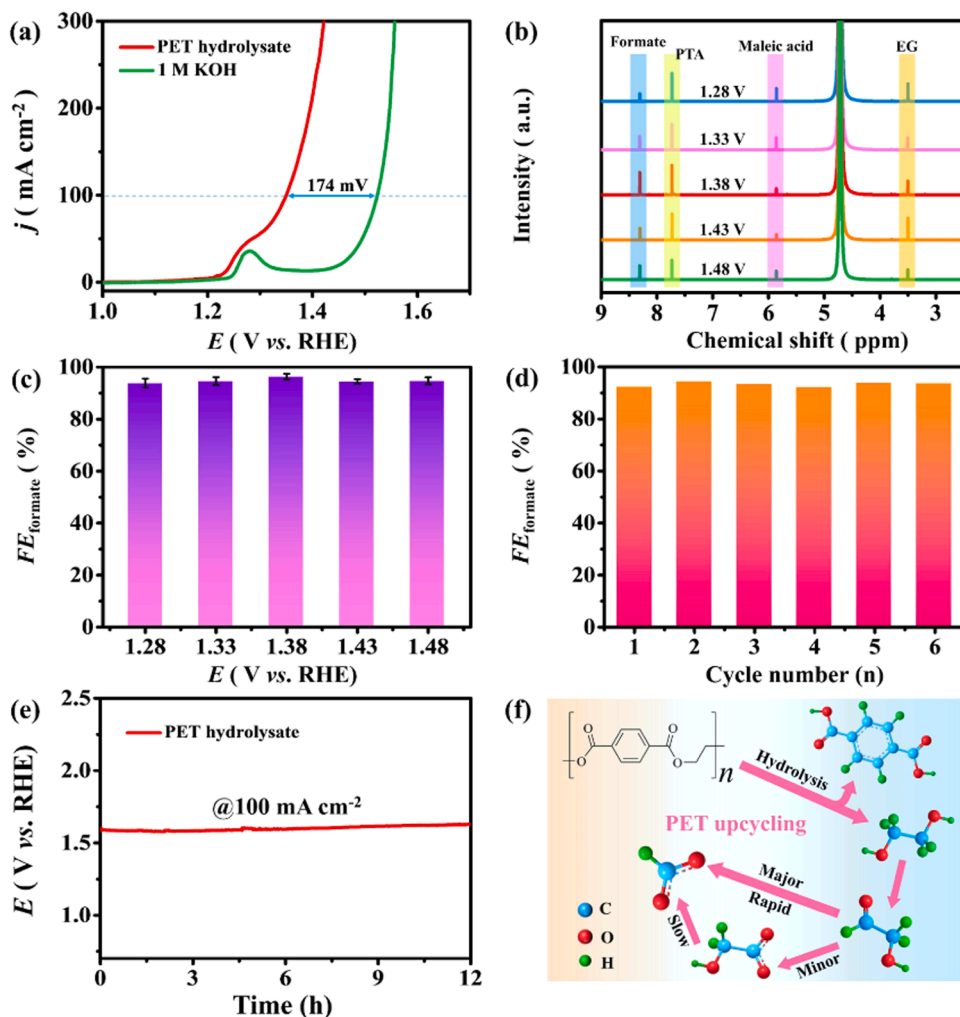


Fig. 5. (a) LSV curves over the Pd-NiTe/NF in PET hydrolysate and 1 M KOH. (b) ¹H NMR spectra of PET hydrolysate and PET hydrolysate oxidation products over the Pd-NiTe/NF at various potentials. (c) Faradaic efficiencies of formate production at various potentials. (d) Faradaic efficiencies of formate production with consecutive six cycles at 1.38 V. (e) Chronoamperometric measurement of Pd-NiTe/NF for PET hydrolysate oxidation. (f) Schematic diagram of PET upcycling process.

and purity of the PET hydrolysate. It can be observed that the formate is barely present in pure PET hydrolysate (Fig. S13). As revealed in Fig. 5c and Fig. S14, Pd-NiTe/NF possesses high FE_{formate} and formate productivity under a varied potential from 1.28 to 1.48 V, with the highest FE of 96.5% and an optimistic formate productivity of 0.3 mmol cm⁻² h⁻¹ at 1.38 V, which outperforms that of reported oxidation performance of PET hydrolysates for the diverse electrocatalysts (Table S3), indicating the exceptional selectivity of the electro-reformed PET hydrolysate oxidation for formate. To further corroborate the PET conversion activity for Pd-NiTe/NF, the turnover frequency (TOF) was determined according to the following formula ($\text{TOF} = n/(t \times N)$, where n is the mole of formate, t is time (h), N is the mole of Pd on the electrode) [53]. The average TOF value of Pd-NiTe/NF is calculated to be 0.5 h⁻¹ at different potentials (Fig. S15), suggesting the higher intrinsic activity for PET hydrolysate oxidation. ¹³C NMR spectrum of post-electrolysis PET hydrolysate also reveals the existence of formate (Fig. S16). An analysis of the electrocatalytic oxidation stability of Pd-NiTe/NF in PET hydrolysate was conducted by recycling it six times at the optimum potential of 1.38 V vs. RHE. As expressed in Fig. 5d, the FE_{formate} shows almost no deterioration after undergoing six successive cycles. Meanwhile, the chronopotentiometric (V - t) curve of Pd-NiTe/NF catalyst in PET hydrolysates also remains stable for 12 h at a current density of 100 mA cm⁻² (Fig. 5e), demonstrating that Pd-NiTe/NF possesses a long-term electrochemical stability. In addition, ¹H NMR data were also carried out to detect the generation of formate at various time points in the stability test (Fig. S17), demonstrating the linear accumulation of formate during the electrocatalytic PET process. Furthermore, a possible

reaction pathway of PET upcycling catalyzed by Pd-NiTe/NF electrode under alkaline conditions is elucidated in Fig. 5f and Fig. S18. The PET waste plastic is hydrolyzed under alkaline conditions to generate EG and PTA, which are further transformed into a more valuable product. Subsequently, the catalytic oxidation of EG to glycolaldehyde takes place, which is cleaved through a rapid C-C oxidation to produce formate. Moreover, a minor fraction of glycolaldehyde undergoes oxidation to glycolic acid followed by slow C-C cleavage to generate formate [17,54].

In the light of the exceptional HER and PET hydrolysate oxidation performances, we focus on demonstrating the proof-of-concept production of H₂, formate, PTA, and KDF from PET plastic. Consequently, as exhibited in Fig. 6a, coupled HER and PET hydrolysate oxidation ((-)HER||PET hydrolysate oxidation(+)) is explored in an H-type cell with a two-electrode system comprised of Pd-NiTe/NF as both the cathodic and anodic catalyst. For comparison, the overall water splitting was also investigated. From the LSV curves in Fig. 6b, it can be distinctly observed that the (-)HER||PET hydrolysate oxidation(+) system presents a lower onset potentials in relative to the (-)HER||OER(+) system, revealing that H₂O at the cathode and PET hydrolysate at the anode can be oxidized and reduced synchronously. The Pd-NiTe/NF requires the voltage of 1.6 V at the current density of 10 mA cm⁻² for (-)HER||PET hydrolysate oxidation(+) system, smaller than that of the water splitting (1.8 V), indicating the advantage of the electrocatalytic coupling strategy. Furthermore, by replacing OER with PET hydrolysate oxidation in the co-electrolysis system, the ability to generate high value-added products and increase energy efficiency in the electrolysis process is

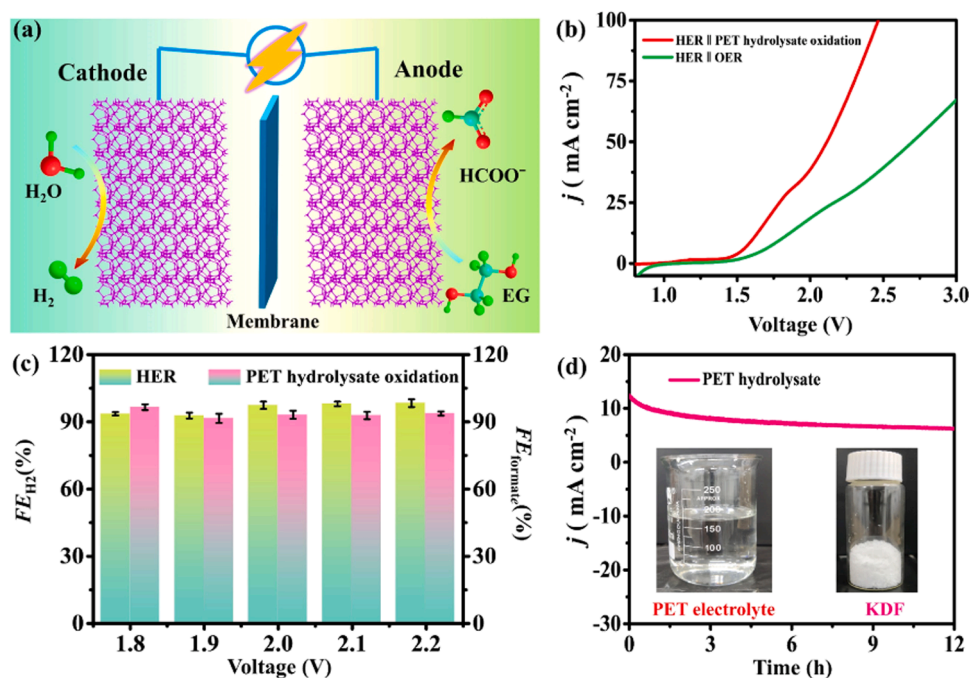


Fig. 6. (a) Schematic illustration of the electrocatalytic system for HER and PET hydrolysate upcycling. (b) LSV curves of Pd-NiTe/NF as cathode and anode in HER||PET hydrolysate oxidation and HER||OER systems. (c) Faradaic efficiencies for the production of H₂ and formate. (d) Chronoamperometric measurement of the HER||PET hydrolysate oxidation over Pd-NiTe/NF||Pd-NiTe/NF in PET hydrolysate. Insets of (d) are the PET electrolyte and the obtained pure KDF.

demonstrated effectively. As shown in Fig. 6c, the FE of H₂ yield over the cathodic HER and the FE_{formate} over the anodic PET hydrolysate oxidation are obtained via the chronoamperometric test at varied voltages from 1.8 to 2.2 V. The optimal 98.6% FE of H₂ generation coupled by the maximum 95.6% FE of the value-added formate production can be achieved, which further illustrates the highly efficient (-)HER||PET hydrolysate oxidation(+) coupled-electrolysis over the bifunctional Pd-NiTe/NF. In addition, a 12-h consecutive electrolysis process reveals the remarkable durability of the coupled system over the Pd-NiTe/NF||Pd-NiTe/NF (Fig. 6d). After the long-term stability test, it can be evidenced by SEM, TEM and HAADF-STEM images that the morphology and structure of Pd-NiTe/NF has no obvious change (Fig. S19). The result of the XRD pattern after the long-term reaction also demonstrates that there is no significant variation in the crystal structure of Pd-NiTe/NF (Fig. S20). To confirm the proof-of-concept production of H₂ and commodity chemicals from the PET plastic over the coupled system, the collected post-electrolysis PET hydrolysate is separated by acidification and filtration to obtain the desired products, as processed in Fig. S21. The regenerated PTA powder could be directly yield in the first step and the white KDF crystal can be acquired through the further condensation and crystallization process of the filtrate liquor, which are identified by the XRD patterns in Fig. S22. The success in regaining PTA and KDF further highlights the feasibility of electrocatalytic PET recycling.

4. Conclusion

In summary, we successfully develop the hierarchical aligned Pd-NiTe/NF nanoarrays heterostructure on the Ni foam, which is employed to establish HER/PET hydrolysate oxidation co-electrolysis system for concurrent production of H₂ and formate. Benefiting from the unique structural advantages, the synergistic effect of the components at the heterointerfaces, and the strongly interfacial electronic interactions of between Pd and NiTe, the as-prepared Pd-NiTe/NF as a bifunctional electrocatalyst exhibits the exceptional activity and decent stability for both HER at cathode and PET hydrolysate oxidation at anode. Impressively, the Pd-NiTe/NF requires the cell voltage of 1.6 V at the current density of 10 mA cm⁻² to drive the coupled two-electrode

system, which is 200 mV lower than that of the water splitting, indicating the advantage of the electrocatalytic coupling strategy. Simultaneously, the coupled electrolyzer also exhibits high FEs for concurrent generation of H₂ (98.6%) and value-added formate (95.6%). The present work may open an electrocatalytic coupled avenue for green hydrogen production and the valorization of PET plastic waste by the design and construction of the cost-effective and high-efficiency bifunctional electrocatalysts.

CRediT authorship contribution statement

Hugang Zhang: Experimental Measurements, Data Analysis, Manuscript Preparation. **Yile Wang:** Experimental Measurements, Data Analysis. **Xinmiao Li:** Data Analysis. **Kai Deng:** Visualization. **Hongjie Yu:** Formal analysis. **You Xu:** Writing – review & editing. **Hongjing Wang:** Supervision, Formal analysis. **Ziqiang Wang:** Writing – review & editing, Supervision, Project administration, Funding acquisition. **Liang Wang:** Conceptualization, Writing – review & editing, Supervision, Project administration, Funding acquisition.

Declaration of Competing Interest

The authors declare that they have no known competing financial interests or personal relationships that could have appeared to influence the work reported in this paper.

Data availability

No data was used for the research described in the article.

Acknowledgements

This work was financially supported by the National Natural Science Foundation of China (Nos. 21972126, 21978264, 21905250, 22278369, 22372148 and 22308330), Natural Science Foundation of Zhejiang Province (No. LQ22B030012 and LQ23B030010), and China Post-doctoral Science Foundation (2021M702889).

Appendix A. Supporting information

Supplementary data associated with this article can be found in the online version at [doi:10.1016/j.apcatb.2023.123236](https://doi.org/10.1016/j.apcatb.2023.123236).

References

- [1] A. Stubbins, K.L. Law, S.E. Muñoz, T.S. Bianchi, L. Zhu, Plastics in the earth system, *Science* 373 (2021) 51–55, <https://doi.org/10.1126/science.abb0354>.
- [2] M. MacLeod, H.P.H. Arp, M.B. Tekman, A. Jahnke, The global threat from plastic pollution, *Science* 373 (2021) 61–65, <https://doi.org/10.1126/science.abg5433>.
- [3] H. Su, T. Li, S. Wang, L. Zhu, Y. Hu, Low-temperature upcycling of PET waste into high-purity H₂ fuel in a one-pot hydrothermal system with in situ CO₂ capture, *J. Hazard. Mater.* 443 (2023), 130120, <https://doi.org/10.1016/j.jhazmat.2022.130120>.
- [4] H. Zhou, Y. Ren, Z. Li, M. Xu, Y. Wang, R. Ge, X. Kong, L. Zheng, H. Duan, Electrocatalytic upcycling of polyethylene terephthalate to commodity chemicals and H₂ fuel, *Nat. Commun.* 12 (2021) 4679, <https://doi.org/10.1038/s41467-021-25048-x>.
- [5] S. Behera, S. Dinda, R. Saha, B. Mondal, Quantitative electrocatalytic upcycling of polyethylene terephthalate plastic and its oligomer with a cobalt-based one-dimensional coordination polymer having open metal sites along with coproduction of hydrogen, *ACS Catal.* 13 (2023) 469–474, <https://doi.org/10.1021/acscatal.2c05270>.
- [6] C. Wang, H. Han, Y. Wu, D. Astruc, Nanocatalyzed upcycling of the plastic wastes for a circular economy, *Coord. Chem. Rev.* 458 (2022), 214422, <https://doi.org/10.1016/j.ccr.2022.214422>.
- [7] T. Ren, Z. Yu, H. Yu, K. Deng, Z. Wang, X. Li, H. Wang, L. Wang, Y. Xu, Sustainable ammonia electrosynthesis from nitrate wastewater coupled to electrocatalytic upcycling of polyethylene terephthalate plastic waste, *ACS Nano* 17 (2023) 12422–12432, <https://doi.org/10.1021/acsnano.3c01862>.
- [8] H. Zhou, Y. Wang, Y. Ren, Z. Li, X. Kong, M. Shao, H. Duan, Plastic waste valorization by leveraging multidisciplinary catalytic technologies, *ACS Catal.* 12 (2022) 9307–9324, <https://doi.org/10.1021/acscatal.2c02775>.
- [9] V. Tournier, C.M. Topham, A. Gilles, B. David, C. Folgoas, E. Moya-Leclair, E. Kamionka, M.L. Desrousseaux, H. Texier, S. Gavalda, M. Cot, E. Guémard, M. Dalibey, J. Nomme, G. Cioci, S. Barbe, M. Chateau, I. André, S. Duquesne, A. Marty, An engineered PET depolymerase to break down and recycle plastic bottles, *Nature* 580 (2020) 216–219, <https://doi.org/10.1038/s41586-020-2149-4>.
- [10] R. Wei, T. Tiso, J. Bertling, K. O'Connor, L.M. Blank, U.T. Bornscheuer, Possibilities and limitations of biotechnological plastic degradation and recycling, *Nat. Catal.* 3 (2020) 867–871, <https://doi.org/10.1038/s41929-020-00521-w>.
- [11] K. Zheng, Y. Wu, Z. Hu, S. Wang, X. Jiao, J. Zhu, Y. Sun, Y. Xie, Progress and perspective for conversion of plastic wastes into valuable chemicals, *Chem. Soc. Rev.* 52 (2023) 8–29, <https://doi.org/10.1039/D2CS00688J>.
- [12] F. Ma, S. Wang, X. Gong, X. Liu, Z. Wang, P. Wang, Y. Liu, H. Cheng, Y. Dai, Z. Zheng, B. Huang, Highly efficient electrocatalytic hydrogen evolution coupled with upcycling of microplastics in seawater enabled via Ni₃N/WsN₄ janus nanostructures, *Appl. Catal. B Environ.* 307 (2022), 121198, <https://doi.org/10.1016/j.apcatb.2022.121198>.
- [13] N. Wang, X. Li, M.-K. Hu, W. Wei, S.-H. Zhou, X.-T. Wu, Q.-L. Zhu, Ordered macroporous superstructure of bifunctional cobalt phosphide with heteroatomic modification for paired hydrogen production and polyethylene terephthalate plastic recycling, *Appl. Catal. B Environ.* 316 (2022), 121667, <https://doi.org/10.1016/j.apcatb.2022.121667>.
- [14] J. Wang, X. Li, M. Wang, T. Zhang, X. Chai, J. Lu, T. Wang, Y. Zhao, D. Ma, Electrocatalytic valorization of poly(ethylene terephthalate) plastic and CO₂ for simultaneous production of formic acid, *ACS Catal.* 12 (2022) 6722–6728, <https://doi.org/10.1021/acscatal.2c01128>.
- [15] M. Du, Y. Zhang, S. Kang, X. Guo, Y. Ma, M. Xing, Y. Zhu, Y. Chai, B. Qiu, Trash to treasure: photoreforming of plastic waste into commodity chemicals and hydrogen over MoS₂-tipped CdS nanorods, *ACS Catal.* 12 (2022) 12823–12832, <https://doi.org/10.1021/acscatal.2c03605>.
- [16] J. Tian, C. Cao, D.-D. Ma, S.-G. Han, Y. He, X.-T. Wu, Q.-L. Zhu, Killing two birds with one stone: selective oxidation of small organic molecule as anodic reaction to boost CO₂ electrolysis, *Small Struct.* 3 (2021), 2100134, <https://doi.org/10.1002/sstr.202100134>.
- [17] J. Wang, X. Li, T. Zhang, Y. Chen, T. Wang, Y. Zhao, Electro-reforming polyethylene terephthalate plastic to co-produce valued chemicals and green hydrogen, *J. Phys. Chem. Lett.* 13 (2022) 622–627, <https://doi.org/10.1021/acs.jpclett.1c03658>.
- [18] Q. Zhou, R. Sun, Y. Ren, R. Tian, J. Yang, H. Pang, K. Huang, X. Tian, L. Xu, Y. Tang, Reactive template-derived interfacial engineering of CoP/CoO heterostructured porous nanotubes towards superior electrocatalytic hydrogen evolution, *Carbon Energy* 5 (2023), e273, <https://doi.org/10.1002/cey.2.273>.
- [19] Y. Qiu, J. Liu, M. Sun, J. Yang, J. Liu, X. Zhang, X. Liu, L. Zhang, Rational design of electrocatalyst with abundant Co/MoN heterogeneous domains for accelerating hydrogen evolution reaction, *Chin. J. Struct. Chem.* 41 (2022) 2207040–2207045, <https://doi.org/10.14102/j.cnki.0254-5861.2022-0144>.
- [20] L. Jiao, W. Wei, X. Li, C.-B. Hong, S.-G. Han, M.I. Khan, Q.-L. Zhu, Value-added formate production from selective ethylene glycol oxidation based on cost-effective self-supported MOF nanosheet arrays, *Rare Met.* 41 (2022) 3654–3661, <https://doi.org/10.1007/s12598-022-02072-4>.
- [21] Z. Zheng, D. Wu, G. Chen, N. Zhang, H. Wan, X. Liu, R. Ma, Microcrystallization and lattice contraction of NiFe LDHs for enhancing water electrocatalytic oxidation, *Carbon Energy* 4 (2022) 901–913, <https://doi.org/10.1002/cey.2.215>.
- [22] X. Qiao, X. Yin, L. Wen, X. Chen, J. Li, H. Ye, X. Huang, W. Zhao, T. Wang, Variable nanosheets for highly efficient oxygen evolution reaction, *Chem* 8 (2022) 3241–3251, <https://doi.org/10.1016/j.chempr.2022.08.007>.
- [23] J. Zhang, W.-J. Jiang, S. Niu, H. Zhang, J. Liu, H. Li, G.-F. Huang, L. Jiang, W.-Q. Huang, J.-S. Hu, W. Hu, Organic small molecule activates transition metal foam for efficient oxygen evolution reaction, *Adv. Mater.* 32 (2020), 1906015, <https://doi.org/10.1002/adma.201906015>.
- [24] T. Wang, X. Cao, L. Jiao, Progress in hydrogen production coupled with electrochemical oxidation of small molecules, *Angew. Chem. Int. Ed.* 61 (2022), e202213328, <https://doi.org/10.1002/anie.202213328>.
- [25] Y. Li, X. Wei, L. Chen, J. Shi, Electrocatalytic hydrogen production trilogy, *Angew. Chem. Int. Ed.* 60 (2021) 19550–19571, <https://doi.org/10.1002/anie.202009854>.
- [26] K. Yin, Y. Chao, F. Lv, L. Tao, W. Zhang, S. Lu, M. Li, Q. Zhang, L. Gu, H. Li, S. Guo, One nanometer PtIr nanowires as high-efficiency bifunctional catalysts for electrosynthesis of ethanol into high value-added multicarbon compound coupled with hydrogen production, *J. Am. Chem. Soc.* 143 (2021) 10822–10827, <https://doi.org/10.1021/jacs.1c04626>.
- [27] X. Jiang, Z. Dong, Q. Zhang, G.-R. Xu, J. Lai, Z. Li, L. Wang, Decoupled hydrogen evolution from water/seawater splitting by integrating ethylene glycol oxidation on PtRh_{0.02}/Rh nanowires with Rh atom modification, *J. Mater. Chem. A* 10 (2022) 20571–20579, <https://doi.org/10.1039/D2TA05469H>.
- [28] J. Zhou, C. Zhu, Y. Zhou, J. Dong, P. Li, Z. Zhang, Z. Wang, Y.-C. Lin, J. Shi, R. Zhang, Y. Zheng, H. Yu, B. Tang, F. Liu, L. Wang, L. Liu, G.-B. Liu, W. Hu, Y. Gao, H. Yang, W. Gao, L. Lu, Y. Wang, K. Suenaga, G. Liu, F. Ding, Y. Yao, Z. Liu, Composition and phase engineering of metal chalcogenides and phosphorus chalcogenides, *Nat. Mater.* 22 (2023) 450–458, <https://doi.org/10.1038/s41563-022-01291-5>.
- [29] J. Tian, C. Cao, Y. He, M.I. Khan, X.-T. Wu, Q.-L. Zhu, Engineering hierarchical quaternary superstructure of an integrated MOF-derived electrode for boosting urea electrooxidation assisted water electrolysis, *Green. Energy Environ.* (2022), <https://doi.org/10.1016/j.gee.2022.05.001>.
- [30] B.B. Lynch, A.P. Kelliher, B.D. Anderson, A. Japit, M.A. Spencer, M.H. Rizvi, M. F. Sarac, V. Augustyn, J.B. Tracy, Sulfidation and selenidation of nickel nanoparticles, *Carbon Energy* 3 (2021) 582–589, <https://doi.org/10.1002/cey.2.83>.
- [31] X. Hou, T. Jiang, X. Xu, X. Wang, J. Zhou, H. Xie, Z. Liu, L. Chu, M. Huang, Coupling of NiFe-based metal-organic framework nanosheet arrays with embedded Fe-Ni₃S₂ clusters as efficient bifunctional electrocatalysts for overall water splitting, *Chin. J. Struct. Chem.* 41 (2022) 2207074–2207080, <https://doi.org/10.14102/j.cnki.0254-5861.2022-0145>.
- [32] Y. He, L. Liu, C. Zhu, S. Guo, P. Golani, B. Koo, P. Tang, Z. Zhao, M. Xu, C. Zhu, P. Yu, X. Zhou, C. Gao, X. Wang, Z. Shi, L. Zheng, J. Yang, B. Shin, J. Arbiol, H. Duan, Y. Du, M. Heggen, R.E. Dunin-Borkowski, W. Guo, Q.-J. Wang, Z. Zhang, Z. Liu, Amorphizing noble metal chalcogenide catalysts at the single-layer limit towards hydrogen production, *Nat. Catal.* 5 (2022) 212–221, <https://doi.org/10.1038/s41929-022-00753-y>.
- [33] J. Li, L. Li, X. Ma, X. Han, C. Xing, X. Qi, R. He, J. Arbiol, H. Pan, J. Zhao, J. Deng, Y. Zhang, Y. Yang, A. cabot, selective ethylene glycol oxidation to formate on nickel selenide with simultaneous evolution of hydrogen, *Adv. Sci.* (2023), 2300841, <https://doi.org/10.1002/advs.202300841>.
- [34] I.E. Castelli, M. Zorko, T.M. Østergaard, P.F.B.D. Martins, P.P. Lopes, B. K. Antonopoulos, F. Maglia, N.M. Markovic, D. Strmcnik, J. Rossmeisl, The role of an interface in stabilizing reaction intermediates for hydrogen evolution in aprotic electrolytes, *Chem. Sci.* 11 (2020) 3914–3922, <https://doi.org/10.1039/C9SC05768D>.
- [35] A. Louidice, R. Buonsanti, Reaction intermediates in the synthesis of colloidal nanocrystals, *Nat. Synth.* 1 (2022) 344–351, <https://doi.org/10.1038/s44160-022-00056-x>.
- [36] Y. Zhang, Y. Lin, T. Duan, L. Song, Interfacial engineering of heterogeneous catalysts for electrocatalysis, *Mater. Today* 48 (2021) 115–134, <https://doi.org/10.1016/j.mattod.2021.02.004>.
- [37] L. Hu, X. Zeng, X. Wei, H. Wang, Y. Wu, W. Gu, L. Shi, C. Zhu, Interface engineering for enhancing electrocatalytic oxygen evolution of NiFe LDH/NiTe heterostructures, *Appl. Catal. B Environ.* 273 (2020), 119014, <https://doi.org/10.1016/j.apcatb.2020.119014>.
- [38] Q. Mao, W. Wang, K. Deng, H. Yu, Z. Wang, Y. Xu, X. Li, L. Wang, H. Wang, Low-content Pt-triggered the optimized d-band center of Rh metallene for energy-saving hydrogen production coupled with hydrazine degradation, *J. Energy Chem.* 85 (2023) 58–66, <https://doi.org/10.1016/j.jechem.2023.06.005>.
- [39] P. Chen, Y. Tong, C. Wu, Y. Xie, Surface/interfacial engineering of inorganic low-dimensional electrode materials for electrocatalysis, *Acc. Chem. Res.* 51 (2018) 2857–2866, <https://doi.org/10.1021/acs.accounts.8b00266>.
- [40] J. Feng, F. Lv, W. Zhang, P. Li, K. Wang, C. Yang, B. Wang, Y. Yang, J. Zhou, F. Lin, G.-C. Wang, S. Guo, Iridium-based multimetallic porous hollow nanocrystals for efficient overall-water-splitting catalysis, *Adv. Mater.* 29 (2017), 1703798, <https://doi.org/10.1002/adma.201703798>.
- [41] H. Sun, L. Li, M. Humayun, H. Zhang, Y. Bo, X. Ao, X. Xu, K. Chen, K. Ostrikov, K. Huo, W. Zhang, C. Wang, Y. Xiong, Achieving highly efficient pH-universal hydrogen evolution by superhydrophilic amorphous/crystalline Rh(OH)₃/NiTe coaxial nanorod array electrode, *Appl. Catal. B Environ.* 305 (2022), 121088, <https://doi.org/10.1016/j.apcatb.2022.121088>.
- [42] Z. Xue, X. Li, Q. Liu, M. Cai, K. Liu, M. Liu, Z. Ke, X. Liu, G. Li, Interfacial electronic structure modulation of NiTe nanoarrays with NiS nanodots facilitates

- electrocatalytic oxygen evolution, *Adv. Mater.* 31 (2019), 1900430, <https://doi.org/10.1002/adma.201900430>.
- [43] J. Lee, C. Kim, K. Choi, J. Seo, Y. Choi, W. Choi, Y.-M. Kim, H.Y. Jeong, J.H. Lee, G. Kim, H. Park, In-situ coalesced vacancies on MoSe₂ mimicking noble metal: unprecedented tafel reaction in hydrogen evolution, *Nano Energy* 63 (2019), 103846, <https://doi.org/10.1016/j.nanoen.2019.06.042>.
- [44] H. Zhang, S. Liu, P. Tian, Y. Mao, Y. Xu, H. Wang, X. Li, Z. Wang, L. Wang, Mesoporous RhTe nanowires towards all-pH-value hydrogen evolution electrocatalysis, *Chem. Eng. J.* 435 (2022), 134798, <https://doi.org/10.1016/j.cej.2022.134798>.
- [45] H. Sun, J.-M. Yang, J.-G. Li, Z. Li, X. Ao, Y.-Z. Liu, Y. Zhang, Y. Li, C. Wang, J. Tang, Synergistic coupling of NiTe nanoarrays with RuO₂ and NiFe-LDH layers for high-efficiency electrochemical-/photovoltage-driven overall water splitting, *Appl. Catal. B Environ.* 272 (2020), 118988, <https://doi.org/10.1016/j.apcatb.2020.118988>.
- [46] H. Zhang, S. Liu, Z. Wang, X. Li, K. Deng, H. Yu, X. Wang, Y. Xu, H. Wang, L. Wang, Ni-doped hyperbranched PdCu nanocrystals for efficient electrocatalytic borohydride oxidation, *J. Mater. Chem. A* 10 (2022) 24694–24700, <https://doi.org/10.1039/d2ta07066a>.
- [47] Y. Li, H. Guo, J. Zhao, Y. Zhang, L. Zhao, R. Song, Te-doped NiFe₂O₄ stabilized by amorphous carbon layers derived from one-step topological transitions of NiFe LDHs with significantly enhanced oxygen evolution reaction, *Chem. Eng. J.* 464 (2023), 142604, <https://doi.org/10.1016/j.cej.2023.142604>.
- [48] Z. Wang, H. Zhang, S. Liu, Z. Dai, P. Wang, Y. Xu, X. Li, L. Wang, H. Wang, Engineering bunched RhTe nanochains for efficient methanol oxidation electrocatalysis, *Chem. Commun.* 56 (2020) 13595–13598, <https://doi.org/10.1039/d0cc05720g>.
- [49] S. Liu, H. Zhang, H. Yu, K. Deng, Z. Wang, Y. Xu, L. Wang, H. Wang, Defect-rich PdIr bimetallic nanoribbons with interatomic charge localization for isopropanol-assisted seawater splitting, *Small* 19 (2023), 2300388, <https://doi.org/10.1002/sml.202300388>.
- [50] H. Zhang, X. Li, Y. Wang, K. Deng, H. Yu, Y. Xu, H. Wang, Z. Wang, L. Wang, Porous PdZn bimetallic for oxygen reduction electrolysis, *Appl. Catal. B Environ.* 338 (2023), 123006, <https://doi.org/10.1016/j.apcatb.2023.123006>.
- [51] R.R. Rao, S. Corby, A. Bucci, M. García-Tecedor, C.A. Mesa, J. Rossmeisl, S. Giménez, J. Lloret-Fillol, I.E.L. Stephens, J.R. Durrant, Spectroelectrochemical analysis of the water oxidation mechanism on doped nickel oxides, *J. Am. Chem. Soc.* 144 (2022) 7622–7633, <https://doi.org/10.1021/jacs.1c08152>.
- [52] J. Xie, L. Gao, S. Cao, W. Liu, F. Lei, P. Hao, X. Xia, B. Tang, Copper-incorporated hierarchical wire-on-sheet α -Ni(OH)₂ nanoarrays as robust trifunctional catalysts for synergistic hydrogen generation and urea oxidation, *J. Mater. Chem. A* 7 (2019) 13577–13584, <https://doi.org/10.1039/C9TA02891A>.
- [53] Y. Yan, H. Zhou, S.M. Xu, J. Yang, P. Hao, X. Cai, Y. Ren, M. Xu, X. Kong, M. Shao, Z. Li, H. Duan, Electrocatalytic upcycling of biomass and plastic wastes to biodegradable polymer monomers and hydrogen fuel at high current densities, *J. Am. Chem. Soc.* 145 (2023) 6144–6155, <https://doi.org/10.1021/jacs.2c11861>.
- [54] F. Liu, X. Gao, R. Shi, E.C.M. Tse, Y. Chen, A general electrochemical strategy for upcycling polyester plastics into added-value chemicals by a CuCo₂O₄ catalyst, *Green. Chem.* 24 (2022) 6571–6577, <https://doi.org/10.1039/d2gc02049a>.